Ecodesign of 3D volumetric fiber-composite structures with topology optimization

Gustavo Asai, Chintan Jansari, Frédéric Lachaud, Kunal Masania, Joseph Morlier

Ecodesign of 3D volumetric fiber-composite structures with topology optimization

Gustavo Asai [a,b], Chintan Jansari [d], Frédéric Lachaud [c], Kunal Masania [d], Joseph Morlier [c,*]

[a] Instituto Tecnológico de Aeronáutica, São José dos Campos, 12228-900, São Paulo, Brazil
[b] ISAE-SUPAERO, Université de Toulouse, DMSM, Toulouse, 31055, France
[c] ICA, Université de Toulouse, ISAE-SUPAERO, MINES ALBI, UPS, INSA, CNRS, Toulouse, 31055, France
[d] Shaping Matter Lab, Faculty of Aerospace Engineering, Delft University of Technology, Delft, 2629 HS, The Netherlands

Dataset link: https://github.com/mid2SUPAERO/SOMP_Ansys

Keywords:
Topology optimization
Ecodesign
3D printing
Manufacturing constraints

A B S T R A C T

Design for composite material additive manufacturing is governed by multiple process variables that can be computationally expensive to optimize. This is especially true when considering discrete variables, such as the material type to be used, which lead to a lot of possible solutions that have to be evaluated. Here, we propose a workflow for optimizing topology and fiber placement of 3D volumetric structures based on mechanical performance under multiple load cases and environmental impact. An eco-informed material selection from a set fibers and polymers is followed by a methodology to optimize the manufacturing setting. By performing these two steps sequentially, the number of input parameter sets to be tested is reduced in a combinatorial scale, along with the computational cost. The framework can be easily extended by adapting the analyses and holds significant promise for the design of additive manufactured sustainable structures.

1. Introduction

The rapid development of additive manufacturing techniques brings the possibility of creating more complex structural designs. Consequently, the use of computational design tools such as topology optimization has accelerated substantially [1,2].

For isotropic materials, e.g. metallic, the material choice can be decoupled from the topology optimization [3] assuming that the manufacturing process does not play a role in the mechanical properties of the material. This is not the case for composite materials, which are becoming widely used, especially in structural applications often due to their high specific mechanical properties. For composites, the mechanical properties are strongly influenced by geometry, requiring topology optimization to be performed concurrently with material selection.

Another difficulty introduced is the integration of the constraints related to the additive manufacturing process. These include defining the criteria for the feasibility of configurations [4], selecting optimal infill methods [5] and creating the 3D printing path [6,7]. This leads to a complex workflow, often consisting of sequential steps to select material, optimize geometry, constrain for manufacturability, and determine trade-offs to compare designs, which can be cumbersome. To overcome this, in the current work, we aim to:

- Present a new design workflow for 3D fiber-reinforced composite structures that not only can optimize the topology and fiber orientations but also provide a better understanding of their environmental impact and manufacturability.
- Structure each stage of the workflow to get a balance between interdependency and complexity.
- Assess the effectiveness of the proposed workflow with an industrial part design under multiple load conditions.

As evident from the above-mentioned points, the work focuses on three key aspects: topology optimization; CO_2 footprint assessment, and printability assessment. The next subsections provide a concise overview of these aspects before diving into a detailed description of the workflow.

1.1. Life Cycle Assessment (LCA) and ecodesign

Estimating the environmental impact of a product is a complex task, since there are many phases to be taken into account, such as material production, manufacturing, transportation, product use, and end-of-life. In addition there are multiple indicators to be quantified, such as greenhouse gases (GHG) emissions, energy used, and material used [8]. Integrating the Life Cycle Assessment (LCA) into the design process requires a careful selection of the parameters to be optimized and the impact metrics to be evaluated.

* Corresponding author.
E-mail address: joseph.morlier@isae-supaero.fr (J. Morlier).

https://doi.org/10.1016/j.compositesa.2024.108615

Tang et al. [9] present a framework with a rather complete LCA, studying the impact of energy and material consumption of the structure on climate change and human health, while Duriez et al. [10] use GHG emissions as the only metric. However, Tang et al. [9] use a basic topology optimization configuration from commercial software and Duriez et al. [10] focus in making eco-optimized material and process selections.

Both of these frameworks consider isotropic materials and are not directly usable for anisotropic materials. Castro Almeida et al. [11] and Agrawal [12] present then methodologies for optimizing 3D printed composites to minimize the CO_2 footprint of the structure, but a main challenge that remains open is introducing variables of the manufacturing process to the design workflow.

In the context of ecodesign, the use of alternative materials can also be seen as a possible replacement for current materials, since natural fibers and biopolymers present environmental advantages in all life cycle stages [13–15]. However, materials with lower environmental impact generally correlate to lower stiffness, so the trade-off between these two properties must be quantified [16]. Here, we use the Pareto efficiency considering compliance and CO_2 emissions to define a better ecodesign.

1.2. Topology optimization for fiber-reinforced composites

In the past few decades, topology optimization has revolutionized designing, especially for structural applications. In simple terms, topology optimization optimizes the material distribution within a given design domain to achieve the best value of the predefined objective. Various types of topology optimization methods have been proposed till now e.g. density-based, level-set based, feature-based, etc. Interested readers can refer to the following review articles for detailed information about topology optimization [17–19].

Among various topology optimization methods, density-based topology optimization has remained the most popular. It utilizes the density ρ_e assigned to each finite element e in the domain Ω as a design variable. The density variables take values from 0 (void element) to 1 (filled element). To enforce convergence to a predominantly 0/1 configuration, the density is penalized using an interpolation scheme such as the Solid Isotropic Material with Penalization (SIMP [20]). In SIMP, the material properties are obtained using a power law, i.e $E(\rho_e) = \rho_e^p E_0$, where p is a penalization factor (typically $p = 3$). With the penalized material interpolation law, intermediate densities are discouraged in the optimized design.

As industries strive to reduce material consumption and increase efficiency, topology optimization has intersected with material design and manufacturability over time. It has been utilized to design advanced materials such as composites, cellular materials, metamaterials, etc. On the other side, research has also been done to include several real manufacturing constraints in the topology optimization problem. In this article, we focus on fiber-reinforced composites produced through additive manufacturing.

For fiber-reinforced composites, in addition to the topology of the material, the reinforcement also needs to be optimized for better performance. Typically, the reinforcement description is attributed to the fiber orientations. However, it can also include other factors related to fibers such as fiber density. Lee et al. [21] and Kim et al. [22], Li et al. [23] included fiber density in topology optimization sequentially and concurrently, respectively. With the inclusion of extra design variables, these methods could explore larger design spaces and find better designs. However, this advantage comes at a cost of increase complexity and computational cost. Similarly, we can also include such detailed reinforcement descriptions and potentially find a better trade-off among compliance, environmental impact and printability. However, we focus exclusively on fiber orientations to describe reinforcement in the current work, leaving other aspects for future exploration.

For a given domain, the determination of fiber orientations can be performed using various approaches. One of them is Discrete Material Optimization (DMO) [24], which is a useful method for composite laminates, since it is based on a discrete set of possible orientations. However, this approach does not provide means of ensuring fiber continuity in adjacent regions, reducing its suitability for non-uniform orientations.

On the other side of the spectrum, Free Material Optimization (FMO) [25] treats the stiffness tensor components as design variables, increasing the freedom of design, although sometimes leading to infeasible material properties.

The approach chosen to represent material anisotropy while also managing manufacturing constraints is Continuous Fiber Angle Optimization (CFAO), which assigns continuous variables to represent the fiber orientation in each element. This methodology is appropriate in the context of Fused Filament Fabrication (FFF) of short-fiber reinforced polymers [26,27] and can be easily integrated into the SIMP method, adjusted to produce continuous orientations in the domain. However, this approach may introduce new pseudo local minima due to the 2π-periodicity of the angle, so that the angle representations have to be carefully constructed.

We also employ the SIMP integrated CFAO formulation as it offers greater design flexibility compared to FMO. The 2π periodicity issue is addressed through filtering. Moreover, the discontinuous fiber orientations typically seen at the end of the optimization can be readily smoothed using a streamlining algorithm. In the following paragraphs, a standard density topology optimization with the SIMP interpolation scheme and its extension to CFAO are given.

1.2.1. Solid Isotropic Material with Penalization (SIMP)

A density topology optimization approach using the SIMP interpolation scheme that aims to minimize the compliance c can be written as (1) [1], where $\boldsymbol{U}$ and $\boldsymbol{F}$ are the global displacement and force vectors, respectively, $\boldsymbol{K}$ is the global stiffness matrix, N is the number of elements, $\boldsymbol{k_0}$ is the elemental non-penalized stiffness matrix, $\boldsymbol{u_e}$ and $\boldsymbol{k_e} = \rho_e^p \boldsymbol{k_0}$ are the element displacement vector and stiffness matrix, respectively, $\boldsymbol{\rho}$ is the vector of design variables, ρ_{min} is the non-zero minimum density (to avoid singularity), $V(\boldsymbol{\rho})$ and V_0 are the material volume and design domain volume, and f is the prescribed maximum volume fraction.

$$\min_{\boldsymbol{\rho}} c(\boldsymbol{\rho}) = \boldsymbol{U}^T \boldsymbol{K}(\boldsymbol{\rho}) \boldsymbol{U} = \sum_{e=1}^{N} \rho_e^p \boldsymbol{u_e}^T \boldsymbol{k_0} \boldsymbol{u_e}$$
$$\text{subject to } \begin{cases} \frac{V(\boldsymbol{\rho})}{V_0} \leq f \\ \boldsymbol{K}(\boldsymbol{\rho}) \boldsymbol{U} = \boldsymbol{F} \\ 0 < \rho_{min} \leq \rho_e \leq 1, \ e = 1, \ldots, N \end{cases} \tag{1}$$

To avoid the appearance of chequerboard patterns and to ensure the mesh independence of the result, element sensitivities are filtered by a linear decaying convolution filter (2), where r_ρ is a fixed filter radius and $\Delta(e, i)$ is the distance operator between the centers of elements e and i.

$$\rho_e \widetilde{\frac{\partial c}{\partial \rho_e}} = \frac{1}{\sum_i H_{ei}^\rho} \sum_{i=1}^{N} H_{ei}^\rho \rho_i \frac{\partial c}{\partial \rho_i}, \quad H_{ei}^\rho = \max(0, r_\rho - \Delta(e, i)) \tag{2}$$

1.2.2. Continuous Fiber Angle Optimization (CFAO) integrated SIMP

Here, we present the conventional integration of the CFAO method with the SIMP approach. The SIMP method can be extended with CFAO by introducing fiber orientations $\boldsymbol{\theta}$ as design variables. A modified 2D problem where both sets of variables are simultaneously optimized [28] can be given as (3). To avoid using periodic variables, another possible

approach is to define the orientation using the Cartesian components of the orientation vector [29].

$$\min_{\rho,\theta} c(\rho,\theta) = \sum_{e=1}^{N} \rho_e^p \, \boldsymbol{u}_e^T \, \boldsymbol{k_0}(\theta_e) \, \boldsymbol{u}_e$$
$$\text{subject to} \begin{cases} \frac{V(\rho)}{V_0} \le f \\ \boldsymbol{K}(\boldsymbol{\rho},\boldsymbol{\theta})\,\boldsymbol{U} = \boldsymbol{F} \\ 0 < \rho_{min} \le \rho_e \le 1, \;\; e = 1,\dots,N \\ -\frac{\pi}{2} \le \theta_e \le \frac{\pi}{2}, \;\; e = 1,\dots,N \end{cases} \tag{3}$$

In this formulation, an additional filter is necessary to regularize the orientations and create a smoothly varying field that can be more easily converted to a printable structure. There is a wider range of choices for this filter, which is independent of the filter applied to the densities. Within each iteration, it can be applied to the sensitivities [30], the material tensor [31], the angles [32], or the Cartesian projections of the angles [33]. The type of filter can also vary, such as using a Gaussian filter instead of a convolution filter with weights that decay linearly [30].

Although problem definition is quite straightforward in 2D, there are multiple possibilities to extend the problem to 3D, with varying levels of computational cost, manufacturing ease, and design space freedom. Some of them are choosing a printing direction and divide the domain in traditional planar layers [28], using a fiber angle description method based on Archimedean spirals to combine the orientations in different layers and reduce the total number of design variables [34], defining allowable printing planes to make components that can be later assembled [33], slicing the domain in curved layers for spatial printing [7], optimizing geometric primitives (plates, bars) as discrete components [35–38], or introducing design variables to define free 3D fiber orientations by spherical coordinates [32]. In our formulation, we also use the free fiber description (as in [32]), as it provides better design freedom and its implementation is relatively straightforward.

1.3. Outline

The remainder of the article is organized as follows: Section 2 proposes the design workflow, including in-depth information on problem formulation, material models, sensitivity analysis, and metrics for environmental impact & printability. Section 3 showcases the results and discussion, emphasizing the effectiveness of the proposed workflow. Finally, Section 4 summarizes the key conclusions of the work.

2. Methodology

2.1. Proposed workflow

Fig. 1 presents the proposed workflow for optimizing printed structures taking into account mechanical performance, environmental impact, and manufacturability. The workflow consists of two steps: the material selection step and the printing direction selection step.

The material selection step focuses on balancing stiffness & environmental impact. For this, the geometry is optimized using the topology optimization algorithm for various pairs of fiber–matrix material. It outputs both optimized topology and fiber orientations. Based on the results of the topology optimization, the compliance and CO_2 footprint of these optimized designs are evaluated. Since the optimization runs are independent, this procedure can be parallelized with no additional complications. Finally, using the compliance and CO_2 footprint data, the designer can identify the Pareto front designs; and consequently, choose a fiber–matrix material pair that provides a better trade-off between compliance and CO_2 footprint. With this selection, the designer concludes the first step, and proceeds for the second step of the workflow.

The goal of the second — printing direction selection step is to find the direction that leads to the highest stiffness with better printability. The printability is measured by the fraction of material that is self-supported during the 3D printing. To achieve the goal, the designer runs a topology optimization algorithm for various printing directions. Based on topology optimization results, he can identify a design with better stiffness as well as manufacturability. Similar to the last step, the designer can also exploit the Pareto front of compliance and printability score (as shown in Fig. 1).

At the end of the workflow, the outputs are the selected fiber–matrix material pair, the printing direction, and the optimized topology and fiber distribution. This result shall be post-processed to generate the printing instructions.

In both steps, a compliance minimization topology optimization problem is solved for multiple times. A detailed formulation and its implementation, point-wise material definitions, and sensitivity analyses are given in Section 2.2. A detailed flow chart of the topology optimization is also given in Fig. 1. In addition, the CO_2 footprint and printability measures required in Steps 1 and 2, respectively, are introduced in Sections 2.3 and 2.4. Please note that the given compliance problem, almost always utilizes the maximum allowable volume and therefore the CO_2 footprint assessment essentially becomes a material selection due to constant specific CO_2 footprint and density. Therefore, we could decouple material selection (focusing on CO_2 footprint and compliance) from printing direction selection (focusing on printability and compliance). Fully integrating CO_2 footprint and printability into the optimization would require handling discrete parameters within a continuum framework, a complex approach we aim to explore in future work.

2.2. Topology optimization problem

2.2.1. Problem formulation

As mentioned in the introduction section, the considered topology optimization problem involving 3D fiber-reinforced composite is solved using CFAO-SIMP formulation. The CFAO-SIMP formulation can be written as (4) for compliance minimization under multiple load-cases. It considers two sets of angles to define material orientations, $\boldsymbol{\theta}$ and $\boldsymbol{\alpha}$, similarly to Schmidt et al. [32]. The objective function $C(\boldsymbol{\rho},\boldsymbol{\theta},\boldsymbol{\alpha})$ is an aggregation of the compliances c_i of each load case i in the load cases set LC using a p-norm, which is a differentiable approximation of the maximum function (exact for $p \to \infty$).

$$\begin{aligned} \min_{\boldsymbol{\rho},\boldsymbol{\theta},\boldsymbol{\alpha}} C(\boldsymbol{\rho},\boldsymbol{\theta},\boldsymbol{\alpha}) &= \left(\sum_{i \in LC} c_i(\boldsymbol{\rho},\boldsymbol{\theta},\boldsymbol{\alpha})^p \right)^{\frac{1}{p}} \\ &= \left(\sum_{i \in LC} \left(\sum_{e=1}^{N} \rho_e^p \boldsymbol{u}_{e,i}^T \boldsymbol{k_0}(\theta_e,\alpha_e) \boldsymbol{u}_{e,i} \right)^p \right)^{\frac{1}{p}} \\ \text{subject to} & \begin{cases} \frac{V(\rho)}{V_0} - f \le 0 \\ \boldsymbol{K}(\boldsymbol{\rho},\boldsymbol{\theta},\boldsymbol{\alpha})\,\boldsymbol{U}_i = \boldsymbol{F}_i, \;\; \forall i \in LC \\ 0 < \rho_{min} \le \rho_e \le 1, \;\; e = 1,\dots,N \\ -\frac{\pi}{2} \le \theta_e \le \frac{\pi}{2}, \;\; e = 1,\dots,N \\ -\frac{\pi}{2} \le \alpha_e \le \frac{\pi}{2}, \;\; e = 1,\dots,N \end{cases} \end{aligned} \tag{4}$$

Please note that the penalization factor 'p' and the power 'p' related to the p-norm are different. However, to align with standard notation practices, we keep both as 'p' and they can be distinguished in the current formulation as they do not appear together except here in (4). The 'p' appears in (17) and (18) is the penalization factor, whereas the 'p' appears in (20) is the p-norm power.

Fig. 2 illustrates the reference frames used for the material orientation definition. When optimizing for free oriented fibers, the angles $\boldsymbol{\theta}$ and $\boldsymbol{\alpha}$ correspond to the fiber orientation in a spherical global coordinate system. On the other hand, when optimizing for printing in layers, $\boldsymbol{\alpha}$ is set to zero while $\boldsymbol{\theta}$ are rotations inside the printing plane, which is the plane normal to the printing direction. This model quantifies the influence of the printing direction exclusively by the changes of allowable fiber orientations, neglecting the anisotropy induced by layer adhesion [39].

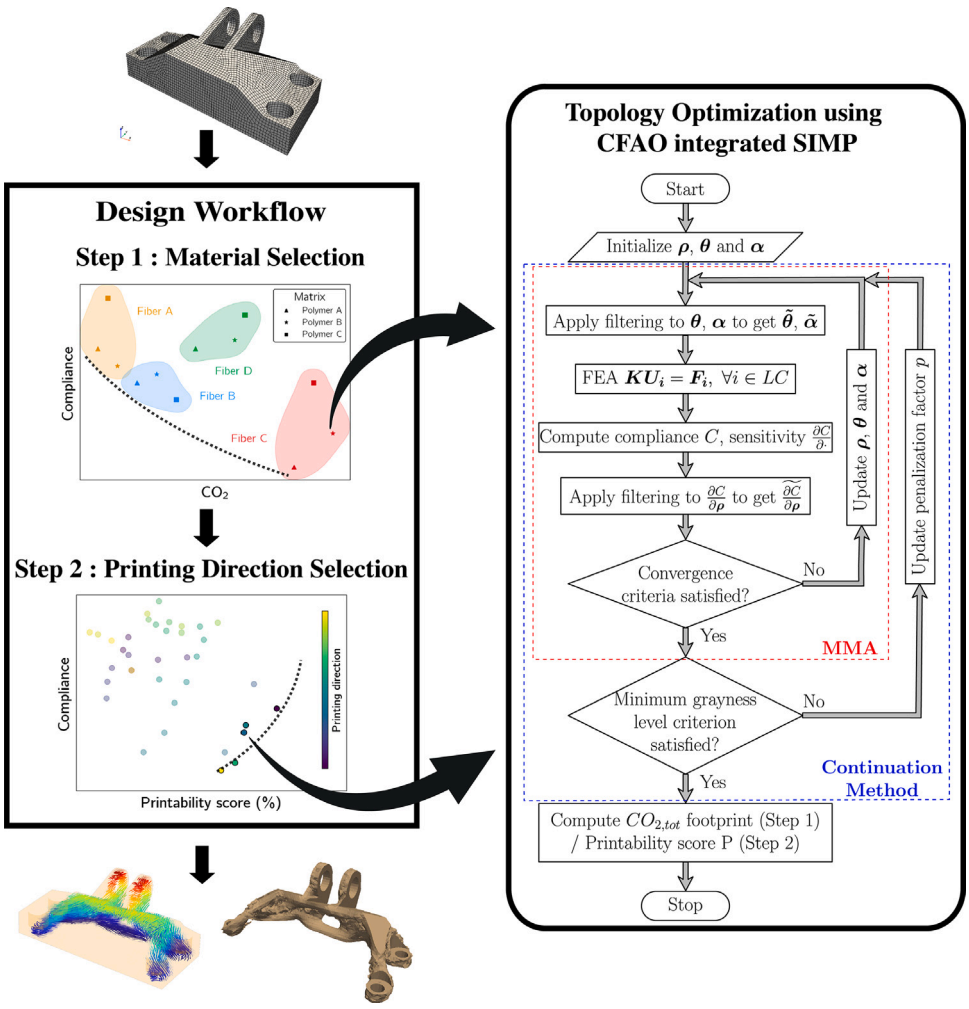

Fig. 1. (Left) Flow chart of the proposed workflow: Starting from an initial design and mechanical loading; Step 1 : multiple designs with different material pairs are optimized, one of them on the Pareto front (of compliance v/s CO_2 footprint) is selected as starting point to the next step, fixing the material to be used; Step 2 : for the selected material pair, multiple designs related to various print setting are optimized, one of them on the Pareto front (of compliance v/s Printability score) is selected as the final optimized design; At the end, design workflow gives an optimized material selection, topology, fiber orientations and printing direction. (Right) Flowchart of the topology optimization problem using CFAO integrated SIMP interpolation scheme. Each data point on the design work flow corresponds to a run of the given topology optimization problem.

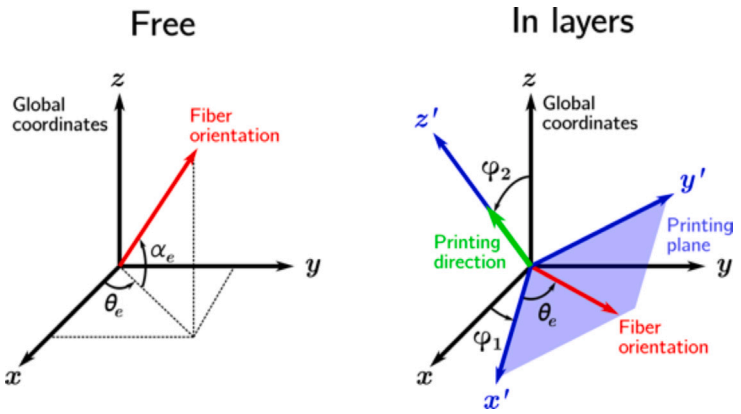

Fig. 2. Reference frames for the fiber orientation definition. φ_1 and φ_2 are the Euler angles of the printing direction vector.

2.2.2. *Filtering*

As mentioned in Sections 1.2.1 and 1.2.2, filtering is necessary for density variables, to ensure mesh-independence & avoid checkerboarding, and for fiber orientations, to regularize the orientations and create a better printable structure. In our work, we filter the sensitivities corresponding to density variables instead of variable themselves, while the fiber orientations variables are directly filtered as in Ypsilantis et al. [40]. Both filters are two separate convolution filters (2) and

(5), respectively. The filters are also adjusted to reduce the contribution from void elements.

$$\begin{bmatrix}\tilde{\theta}_e\\ \tilde{\alpha}_e\end{bmatrix} = \frac{1}{\sum_i H^{\theta}_{ei}\rho_i}\sum_{i\in\Omega} H^{\theta}_{ei}\rho_i \begin{bmatrix}\theta_i\\ \alpha_i\end{bmatrix}, \quad H^{\theta}_{ei} = \max(0, r_\theta - \Delta(e,i)) \tag{5}$$

2.2.3. Material modeling

The materials are modeled as transverse isotropic with fibers aligned with the local x axis, suitable for matrices reinforced by unidirectional fibers. This type of material can be characterized by five independent elastic constants: longitudinal Young modulus E_x, transversal Young modulus E_y, in-plane Poisson's ratio ν_{xy}, out-of-plane Poisson's ratio ν_{yz}, and in-plane shear modulus G_{xy}.

These elastic constants are obtained from the application of the rule of mixtures in a 2-phase (fiber/matrix) micromechanical model. This model is shown to provide results that can work as a fair approximation even for composites of natural origin [41,42]. For a fiber volume fraction of V_f, the material in-plane constants are written as (6)–(9), where E_f, ν_f, G_f are fiber properties and E_m, ν_m, G_m are matrix properties. Moreover, a 3D symmetry constraint is introduced so that ν_{yz} is defined by (10) [43].

$$E_x = E_f V_f + E_m(1-V_f) \tag{6}$$

$$E_y = \frac{E_f E_m}{E_f(1-V_f) + E_m V_f} \tag{7}$$

$$\nu_{xy} = \nu_f V_f + \nu_m(1-V_f) \tag{8}$$

$$G_{xy} = \frac{G_f G_m}{G_f(1-V_f) + G_m V_f} \tag{9}$$

$$\nu_{yz} = \nu_{xy}\frac{1-\nu_{xy}\frac{E_y}{E_x}}{1-\nu_{xy}} \tag{10}$$

The constitutive matrix $\boldsymbol{C}$ for transverse isotropic materials is given by (11) in the local coordinate system. The material orientation with respect to the global coordinates (see Fig. 2) is obtained from successive rotations around the x axis using the rotation matrix $\boldsymbol{T_x}$(12) and around z using $\boldsymbol{T_z}$(13).

$$\boldsymbol{C} = \begin{bmatrix} \frac{1}{E_x} & -\frac{\nu_{xy}}{E_x} & -\frac{\nu_{xy}}{E_x} & 0 & 0 & 0\\ -\frac{\nu_{xy}}{E_x} & \frac{1}{E_y} & -\frac{\nu_{yz}}{E_y} & 0 & 0 & 0\\ -\frac{\nu_{xy}}{E_x} & -\frac{\nu_{yz}}{E_y} & \frac{1}{E_y} & 0 & 0 & 0\\ 0 & 0 & 0 & \frac{2(1+\nu_{yz})}{E_y} & 0 & 0\\ 0 & 0 & 0 & 0 & \frac{1}{G_{xy}} & 0\\ 0 & 0 & 0 & 0 & 0 & \frac{1}{G_{xy}} \end{bmatrix}^{-1} \tag{11}$$

$$\boldsymbol{T_x}(\phi) = \begin{bmatrix} 1 & 0 & 0 & 0 & 0 & 0\\ 0 & \cos^2\phi & \sin^2\phi & -2\sin\phi\cos\phi & 0 & 0\\ 0 & \sin^2\phi & \cos^2\phi & 2\sin\phi\cos\phi & 0 & 0\\ 0 & \sin\phi\cos\phi & -\sin\phi\cos\phi & \cos^2\phi - \sin^2\phi & 0 & 0\\ 0 & 0 & 0 & 0 & \cos\phi & \sin\phi\\ 0 & 0 & 0 & 0 & -\sin\phi & \cos\phi \end{bmatrix} \tag{12}$$

$$\boldsymbol{T_z}(\phi) = \begin{bmatrix} \cos^2\phi & \sin^2\phi & 0 & 0 & 0 & -2\sin\phi\cos\phi\\ \sin^2\phi & \cos^2\phi & 0 & 0 & 0 & 2\sin\phi\cos\phi\\ 0 & 0 & 1 & 0 & 0 & 0\\ 0 & 0 & 0 & \cos\phi & \sin\phi & 0\\ 0 & 0 & 0 & -\sin\phi & \cos\phi & 0\\ \sin\phi\cos\phi & -\sin\phi\cos\phi & 0 & 0 & 0 & \cos^2\phi - \sin^2\phi \end{bmatrix} \tag{13}$$

The general rotated constitutive matrix $\boldsymbol{C_{xyz}}$ in the global coordinate system for an element e is written from the material constitutive matrix $\boldsymbol{C}$ as (14), where φ_1 and φ_2 are the Euler angles of a coordinate system with z axis aligned to the printing direction.

$$\boldsymbol{C_{xyz}}(\alpha_e,\theta_e) = \boldsymbol{T}\,\boldsymbol{C}\,\boldsymbol{T}^T, \quad \boldsymbol{T}(\alpha_e,\theta_e) = \boldsymbol{T_x}(\alpha_e)\,\boldsymbol{T_z}(\theta_e)\,\boldsymbol{T_x}(\varphi_2)\,\boldsymbol{T_z}(\varphi_1) \tag{14}$$

The Euler angles are the same for all elements for a given printing direction and are defined by (15) and (16), where $\boldsymbol{n} = [n_x, n_y, n_z]^T$ is the printing direction unit vector.

$$\varphi_1 = -\arctan\frac{n_x}{n_y} \tag{15}$$

$$\varphi_2 = -\arctan\frac{\sqrt{n_x^2+n_y^2}}{n_z} \tag{16}$$

The final material orientation of an element e is obtained by a rotation of θ_e around the current z axis, in such a manner that the fibers lie on the plane normal to the printing direction vector. To generalize the transformations for the free orientated fibers, an additional rotation of α_e around the new x axis can be performed. In this case, the angles φ_1 and φ_2 can be set to zero and the design variables will represent the fiber orientation in the global coordinate system.

2.2.4. Sensitivity analysis

As to use a gradient-based algorithm, it is necessary to calculate sensitivities of the objective function with respect to the design variables. For densities, the sensitivity for each load case is obtained from the elemental strain energy, which is directly retrieved from Ansys, using (17).

$$\frac{\partial c_i}{\partial \rho_e} = -p\,\rho_e^{p-1}\,\boldsymbol{u}_{e,i}^T\,\boldsymbol{k_0}\,\boldsymbol{u}_{e,i} = -\frac{p}{\rho_e}\underbrace{\boldsymbol{u}_{e,i}^T\,(\rho_e^p\,\boldsymbol{k_0})\,\boldsymbol{u}_{e,i}}_{\substack{2\times\text{ elemental}\\ \text{strain energy}}} \tag{17}$$

The sensitivity on the orientation in (18) depends on $\partial\boldsymbol{k_0}/\partial\theta_e$, which is not directly accessible in Ansys and has to be integrated from the strain–displacement matrix $\boldsymbol{B}$ and the constitutive matrix $\boldsymbol{C}_{xyz}$ using (19). The integrals are evaluated with 2-point Gaussian quadrature, which is exact for the chosen element formulation, which is linear in each natural coordinate. The procedure for α_e is analogous.

$$\frac{\partial c_i}{\partial \theta_e} = -\rho_e^p\,\boldsymbol{u}_{e,i}^T\,\frac{\partial \boldsymbol{k_0}}{\partial \theta_e}\,\boldsymbol{u}_{e,i} \tag{18}$$

$$\frac{\partial \boldsymbol{k_0}}{\partial \theta_e} = \iiint \boldsymbol{B}^T\,\frac{\partial \boldsymbol{C_{xyz}}}{\partial \theta_e}\,\boldsymbol{B}\,d\Omega_e, \quad \frac{\partial \boldsymbol{C_{xyz}}}{\partial \theta_e} = \frac{\partial \boldsymbol{T}}{\partial \theta_e}\,\boldsymbol{C}\,\boldsymbol{T}^T + \boldsymbol{T}\,\boldsymbol{C}\,\frac{\partial \boldsymbol{T}^T}{\partial \theta_e} \tag{19}$$

The final sensitivities are then computed from the individual load cases using (20), obtained by differentiating the objective function $C = (\sum_i c_i^p)^{1/p}$.

$$\frac{\partial C}{\partial \cdot} = \sum_{i\in LC} c_i^{p-1} C^{1-p}\frac{\partial c_i}{\partial \cdot} \tag{20}$$

2.2.5. Implementation

The flowchart provided in Fig. 1 schematizes the implementation of the current optimization method. It uses the Method of Moving Asymptotes (MMA) [44] as optimization algorithm. Additionally, a continuation method is applied on the penalization factor p to improve the quality of the converged solutions. Instead of fixing it throughout the whole optimization, it starts at $p = 1$ and is increased each time a convergence in compliance is achieved. The stopping criterion for the continuation is the greyness level of the design [11], i.e., when the fraction of elements that are neither void nor filled is below a certain level.

The finite element analysis step calls the Ansys linear solver via the PyMAPDL interface [45], allowing a straightforward creation of the mesh and the boundary conditions, which can be time-consuming to perform by hand for complex geometries. The global stiffness matrix assembly step is then abstracted, but the algorithm is still dependent on the elemental stiffness matrices $\boldsymbol{k_0}$. The implementation assumes an 8-node brick element with three degrees of freedom on each node (Ansys element type SOLID185) whose shape functions N_i and strain–displacement matrix $\boldsymbol{B}$ are explicitly computed inside the algorithm.

2.3. CO_2 footprint assessment

The environmental impact of the structure is measured in terms of the mass of CO_2 emitted during material production $CO_{2,mat}$ and during its use $CO_{2,use}$. The value used to compare different designs is the total footprint $CO_{2,tot}$.

The impact of material production is calculated following the methodology proposed by Duriez et al. [3], adapted to composite materials. It depends on the total mass M and the CO_2 intensity of the material $CO^i_{2,mat}$ (mass of CO_2 emitted per mass of material). Its expression for a fiber reinforced composite is given by (22), where ρ_f is the fiber density, $CO^i_{2,f}$ is the fiber CO_2 intensity, ρ_m is the matrix density, $CO^i_{2,m}$ is the matrix CO_2 intensity, and V_f is the fiber volume fraction in the composite material.

The impact of the use phase is calculated as the emissions that would be saved if the component was lighter. Reducing the mass by 1 kg in a long-distance aircraft leads to a reduction of 98.8 tCO_2 during its lifetime [3].

$$CO_{2,tot} = CO_{2,mat} + CO_{2,use} \tag{21}$$

$$CO_{2,mat} = M \cdot CO^i_{2,mat} = M \cdot \frac{\rho_f V_f CO^i_{2,f} + \rho_m (1 - V_f) CO^i_{2,m}}{\rho_f V_f + \rho_m (1 - V_f)} \tag{22}$$

$$CO_{2,use} = M \cdot 98.8\ tCO_2/kg \tag{23}$$

Please note that the compliance optimization problem almost always utilizes the maximum allowed volume, which makes the CO_2 footprint assessment primarily a matter of material selection (see Fig. 6). For future research, it would be valuable to fully integrate the CO_2 footprint using an optimization framework capable of accommodating discrete parameters, such as material selection.

2.4. Printability

In this work, the printability evaluation takes in account only the necessity of adding support material during the printing, following the approach presented by Gaynor and Guest [46], extended to three dimensions.

For each element e, its overhang support neighborhood set N_e^S is defined as the set of the elements below e that are capable of providing support to it during the printing process. N_e^S is composed by the elements whose centers are inside the spherical cone depicted in Fig. 3, defined by the printing direction, the radius r_S, and the minimum self-supporting angle θ_{sup}, that is the minimum angle with respect to the printing plane for which the layers can grow without requiring support material.

The printability of en element e is measured by the support variable ρ_e^S, defined by Eqs. (24), (25), (26), where β_T is the thresholding Heaviside parameter, h is the average element side length, and μ_e^S is the average support provided by its neighborhood. The threshold T is defined so that the printable elements have at least r_S/h elements providing support to them, which is the number of elements that make up a radius of N_e^S.

$$\rho_e^S = \frac{\tanh(\beta_T T) + \tanh(\beta_T (\mu_e^S - T))}{\tanh(\beta_T T) + \tanh(\beta_T (1 - T))} \tag{24}$$

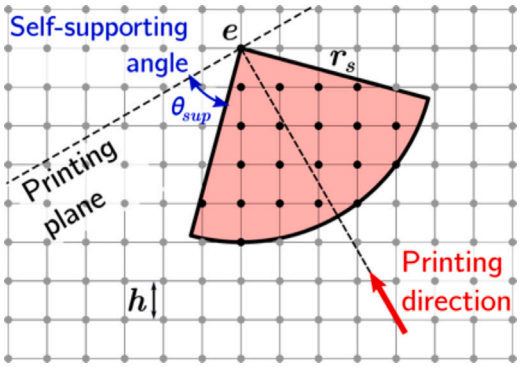

Fig. 3. Overhang support neighborhood set N_e^S.

$$T = \frac{3}{2\pi(1 - \sin\theta_{sup})} \frac{h^2}{r_S^2} \tag{25}$$

$$\mu_e^S = \underset{i \in N_e^S}{\text{mean}} (\rho_i \cdot \rho_i^S) \tag{26}$$

As the value of ρ_e^S depends on ρ_i^S of all elements $i \in N_e^S$, the calculation has to be done layer by layer, which can be computationally expensive since it is hard to parallelize. Finally, a printability score P for the structure is defined in (27) as a weighted average of ρ_e^S over all elements.

$$P = \underset{e \in \Omega}{\text{mean}} (\rho_e \cdot \rho_e^S) \tag{27}$$

3. Results and discussion

The studied problem is the General Electric (GE) jet engine bracket challenge announced in the GrabCAD Community website in 2013 [47]. The initial domain was divided in a mesh with 37 000 hexahedral elements and two load cases: (1) a 35 586 N vertical force and (2) a 37 810 N horizontal force (see Fig. 4). All elements in the regions where the boundary conditions are applied are set to $\rho_e = 1$.

For all optimizations, $r_\rho = 5$ mm, $r_\theta = 7$ mm, $r_S = 1.5\, r_\rho = 7.5$ mm, $\theta_{sup} = 45°$, $\beta_T = 25$, and $n = 8$. The convergence criterion for the compliance is relative change inferior to 0.5% and the stopping criterion for the continuation is greyness level inferior to 30%, with elements being considered grey if their densities are between 0.1 and 0.9. To compare designs that converged at different penalization factors, all compliance values are presented after a correction to the equivalent compliance for $p = 3$.

Due to the non-convexity of the optimization problem, the results are strongly dependent on the initial orientations. To not favor any particular orientation from the start, the initial orientation of each element was randomly chosen, which is a fair heuristic to be used when the best condition is not known [32].

Each data point presented in the next sections represents the optimization results for a single parameter set. Appendix shows a representative example of convergence, as most of them converged after around 40 iterations.

3.1. Material selection

In the material selection step, all the possible combinations of fibers and polymers (fiber volume fraction $V_f = 50\%$) in Table 1 were fed into the algorithm in Fig. 1, with maximum volume fraction of $f = 0.2$ and print direction $+z$. They are also compared to an optimized isotropic design with aluminum 2024 ($E = 70$ GPa, $\nu = 0.3$, $\rho = 2765$ kg/m^3, $CO^i_2 = 8.67$ kg CO_2/kg).

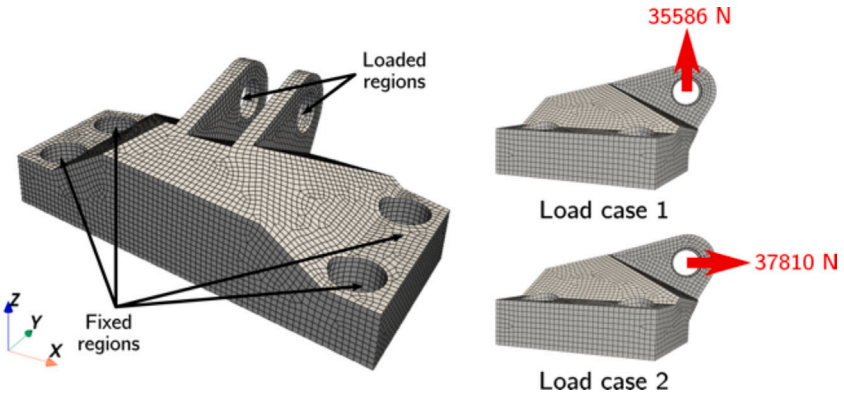

Fig. 4. GE bracket finite element model and two load cases selected from the original challenge [47]. The geometry was simplified to reduce the necessary number of elements.

Table 1
Properties of available materials, taken as average values from Ansys Granta EduPack material database [48].

	Material	ρ (kg/m^3)	E (GPa)	ν	CO_2^i (kg CO_2/kg)
Fibers	Bamboo	700	17.5	0.39	1.0565
	Flax	1470	53.5	0.355	0.44
	Hemp	1490	62.5	0.275	1.6
	HM Carbon	2105	760	0.105	68.1
	S-Glass	2495	89.5	0.22	2.905
Polymers	PLA	1255	3.45	0.39	2.28
	PETG	1270	2.06	0.403	4.375
	Epoxy	1255	2.41	0.399	5.94

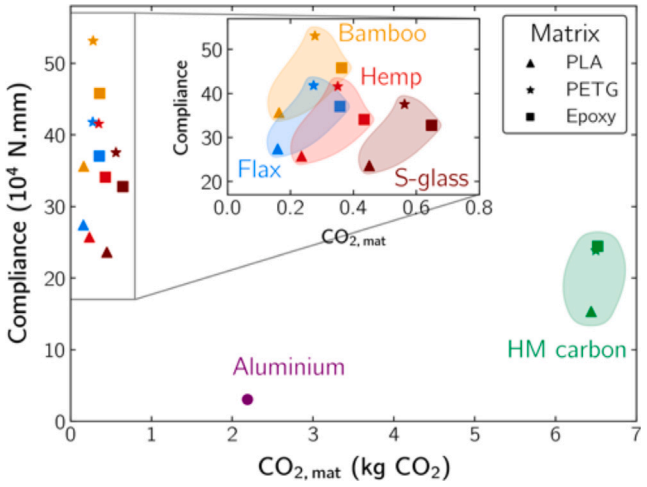

Fig. 5. Compliance versus material production footprint $CO_{2,mat}$ of the optimized designs, grouped by fiber type. Shapes represent the matrices, which introduce similar compliance and footprint changes for all fibers.

Fig. 5 presents the footprint of the material production phase $CO_{2,mat}$ of each of the materials, showing a large gap between the natural fibers and carbon fiber/aluminum. Hence, natural fibers may provide an expressive reduction on environmental impact for use cases where the material production has a more important contribution to the total impact.

This is not always the case since in an aeronautical context, for example, the impact of the use phase is orders of magnitude superior to the impact of the production phase, as observed when comparing the scale of $CO_{2,tot}$ in Fig. 6 and $CO_{2,mat}$ in Fig. 5. Consequently, the CO_2 footprint is driven by the total mass making the specific mechanical properties more relevant than the CO_2 intensity. Herein, as f is fixed, ρ is the main contributor to the environmental impact

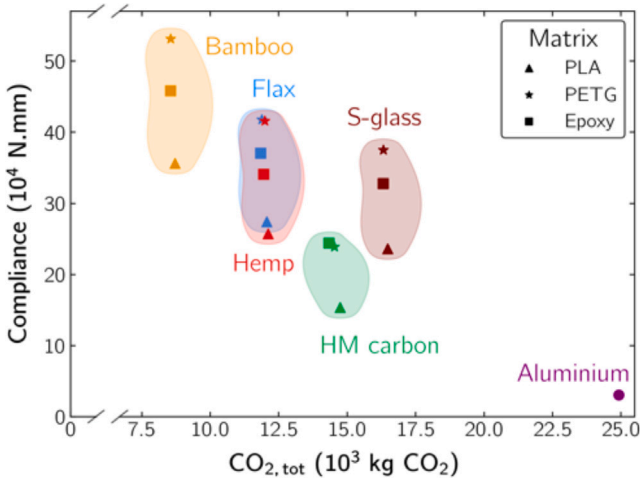

Fig. 6. Compliance versus total footprint $CO_{2,tot}$ of the optimized designs, grouped by fiber type. Shapes represent the matrices, which introduce similar compliance and footprint changes for all fibers.

and the low density natural materials show the lowest $CO_{2,tot}$. The main disadvantage of this type of material is their lower stiffness, here observed as higher compliance values.

There is also a clear separation of the matrix and reinforcement contributions: for the matrices, one can note that PLA is the most Pareto-efficient in simultaneously minimizing compliance and footprint; for the fibers, carbon presents the lowest compliance, bamboo presents the lowest emissions, and the other natural fibers place in between. Results show that, as expected, the final topology depends on the material, especially on the E_x/E_y ratio (see Fig. 7).

Although there are multiple Pareto-optimal materials, the flax/PLA composite was chosen for the next step of the workflow because of its balance between compliance and footprint. These results show that a careful evaluation of the available materials can help obtaining a substantially more eco-efficient structure. Note that other metrics for material selection can be implemented, such as cost, availability, and others. Leaving the volume fraction constraint f as a variable can also provide a more detailed overview for the selection.

All analyses in this step were performed considering the same printing direction, but it also has an influence on the compliance. The next section presents a study on the extent of this influence and on the applicability of using two separate steps.

3.2. Printing direction

A first analysis of the effect of the printing direction was carried out by comparing the compliance and printability score of flax/PLA designs

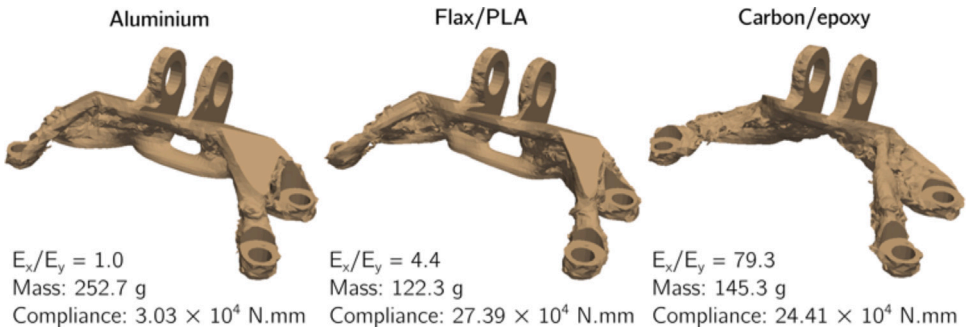

Fig. 7. Isosurfaces of density 0.55 for different materials. The optimized shape is dependent mainly on the material E_x/E_y ratio.

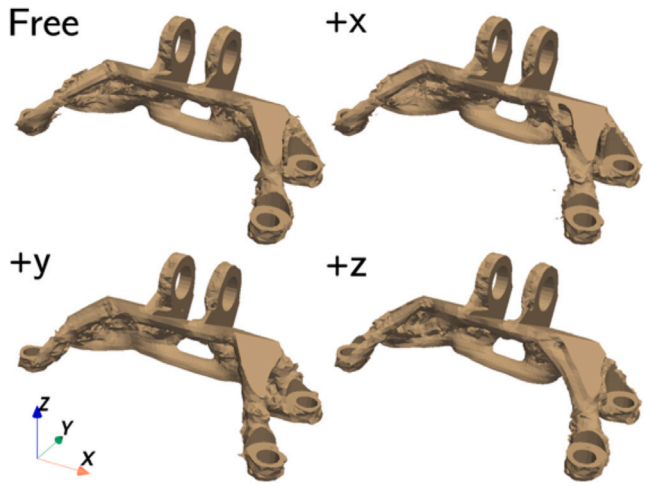

Fig. 8. Isosurfaces of density 0.55 for each printing direction. The optimized topology is similar for all directions, if compared to the variations observed in the previous step.

Table 2
Compliance (combined and single load cases) and printability of optimal designs for each printing direction. Best directions are highlighted in red: $+y$ presents the lowest compliance, while $+z$ presents the highest printability.

Printing direction	Compliance (10^4 N mm)			Printability score (%)
	Combined	Load case 1	Load case 2	
Free	33.86	32.99	27.48	–
$+x$	32.53	32.13	24.20	70.3
+y	**26.38**	25.71	21.38	18.8
+z	27.34	26.80	21.54	**73.7**

optimized for free fibers and for traditional printing along the axes $+x$, $+y$, and $+z$. Fig. 8 and Table 2 summarize the optimized results for each case.

The four topologies are similar, indicating that the compliance differences are indeed a consequence of the fiber placement. Directions $+y$ and $+z$ present lower compliance due their increased fiber continuity, i.e., the domain is divided in less layers that can be printed using longer fiber paths (see Fig. 9). A secondary effect is the presence of fibers aligned to the external force in the dominant load case (case 1 herein, which presents higher compliance). For the $+y$ direction, these fibers can work in tension instead of bending, leading to a lower overall compliance.

Furthermore, the addition the α variables had a negative impact on the performance of the obtained solutions. The additional freedom of the design space is counterbalanced by the presence of many local optima, leading to worse results even though it has a larger design space. Due to the lack of constraints to the design variables, orientations at nearby regions can align to different directions in the first iterations, which later converge to fibers that do not follow the load path, as exemplified in Fig. 10. This issue can be assessed by the fiber path generation during post-processing, but the result remains suboptimal.

It is then clear that the choice of printing direction is a major parameter to be optimized. Fig. 11 shows the compliance and the printability score for several printing angles in the yz plane: 0° corresponds to the $+y$ direction and 90° corresponds to the $+z$ direction.

For this geometry and minimum self-supporting angle configuration, there are multiple Pareto-optimal directions (see Fig. 12). The final choice depends again on the desired trade-off of those properties, which may require the cost evaluation of support material placement, for example.

This result shows that, as expected, the printing direction substantially influences the performance and manufacturability of the optimized geometry. Also, more design freedom does not guarantee better results, highlighting the importance of carrying a careful parametric study along with proper design space restrictions in order to achieve a more practical design.

4. Conclusions

There is an evident separation of the roles of both steps in achieving the optimized results. The material selection step provides a more effective trade-off between stiffness and eco-efficiency. In the same vein, from the Pareto front optimals, we learned that natural bamboo fibers are recommended for superior eco-efficiency and carbon fibers for greater stiffness. On the other hand, flax and hemp fibers can offer a balanced compromise. However, for matrix materials, PLA outperforms PETG and epoxy in terms of both stiffness and eco-efficiency. The selected eco-efficiency in the first step remains almost unchanged in the second step since the compliance minimization problem seeks to use all the material allowed by the volume fraction constraint. The next step of printing direction selection sets a compromise between compliance and printability. For our example, we learned that printing in the +z and +y directions provides stiffer optimized designs than printing in the free or +x directions. Also, +z direction printing design surpasses +y direction one in terms of printability.

The proposed workflow defines these sequential steps as much independent as possible, reducing the procedure's complexity. These steps ease decision-making in designing while using fewer optimization runs. The end result of the workflow is the optimized material selection, fiber orientations, topology and printing direction. A final post-processing using a streamlining algorithm can generate smooth fiber paths before the tool-path generation.

As the LCA is currently being performed only during the material selection, future research may extend the framework by quantifying the impact of different manufacturing configurations. For this purpose, the current environmental and manufacturability analyses can be easily elaborated by including new parameters of the product life cycle and manufacturing processes.

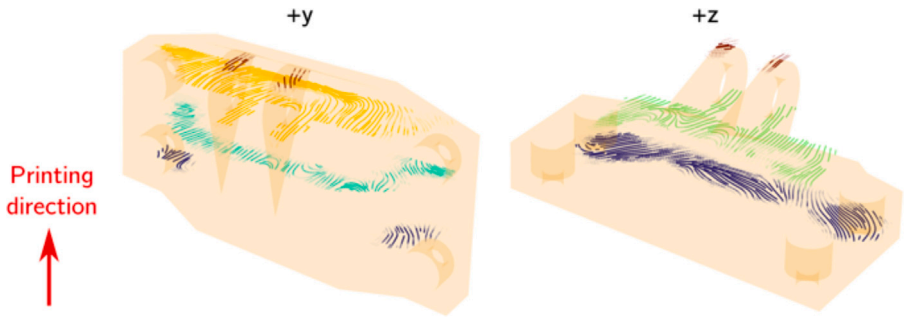

Fig. 9. Optimized fiber distribution, obtained from the elemental orientations by integration using a streamline finding algorithm. Each color represents a layer of the final print.

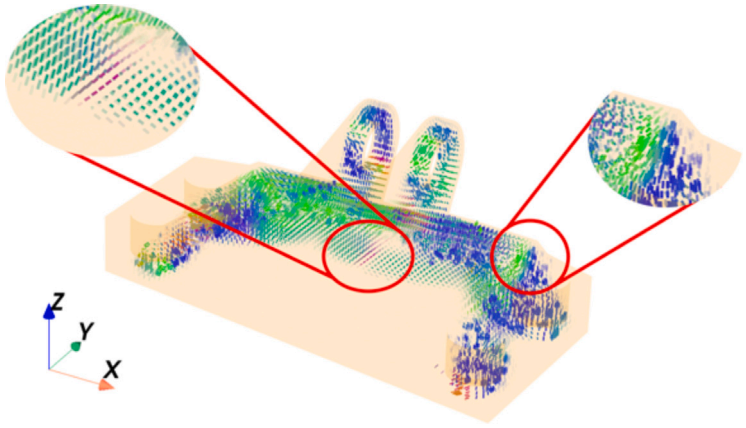

Fig. 10. Fiber orientations at each non-void element in the design optimized with free fibers. Coloring uses the (x, y, z) components of the orientation vector as RGB components: green elements are mostly aligned with the y axis and blue elements are aligned with the z axis.

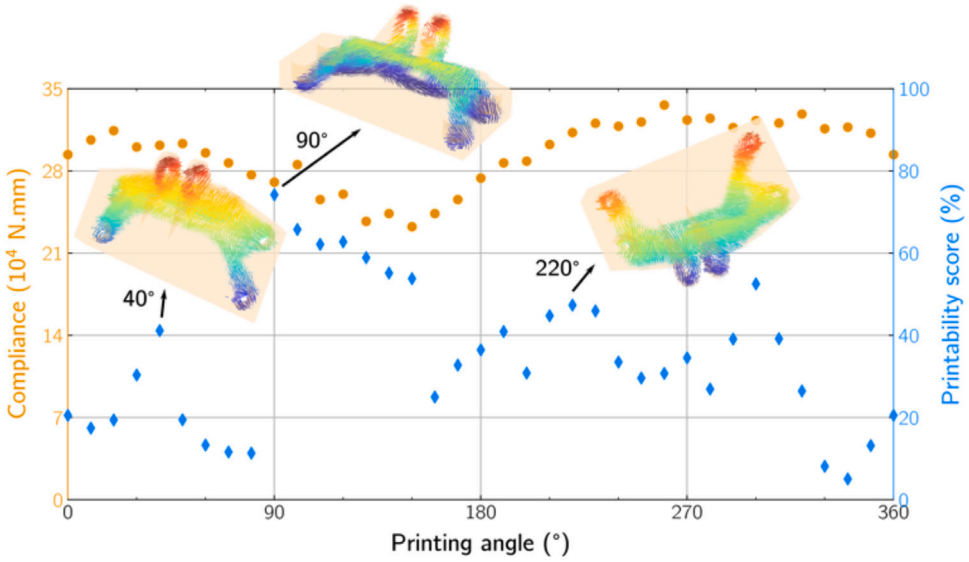

Fig. 11. Compliance and printability of the optimal design as a function of the printing angle (inside yz plane). Fibers are colored by height from the bottom plate. The printability peaks agree with the directions that make the main structural features self-supported.

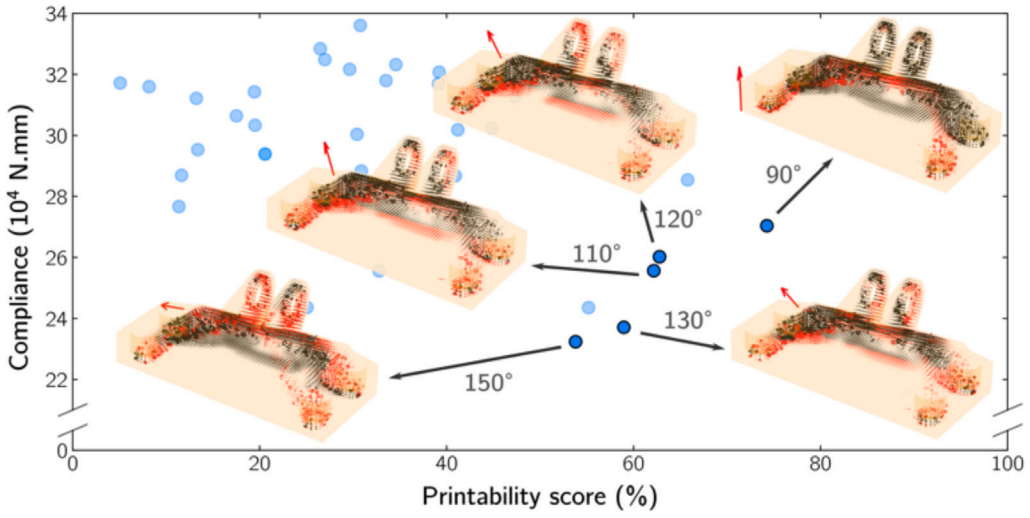

Fig. 12. Pareto-optimal printing angles for compliance minimization and printability maximization. Elements in black are self-supported and elements in red require additional support material to be printed.

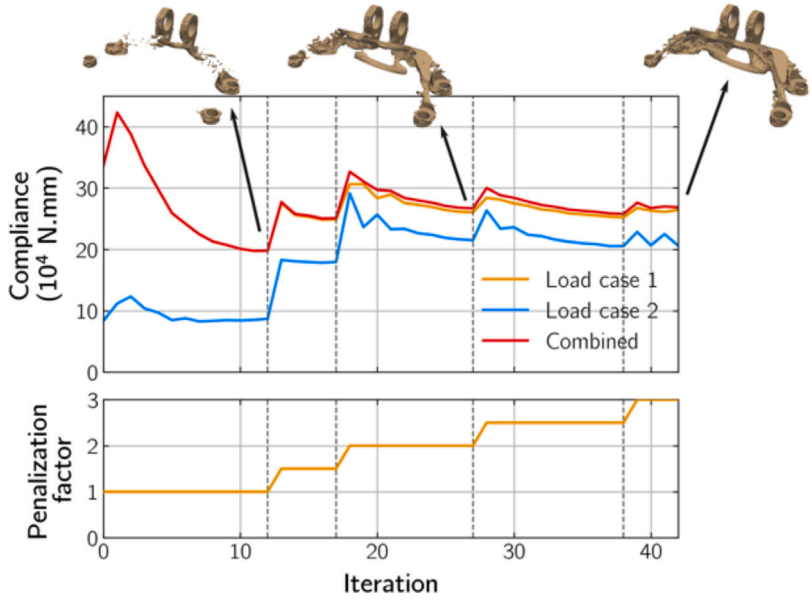

Fig. A.13. Compliance and penalization factor history. Discontinuities in the isosurfaces of density 0.55 indicate the presence of low-density grey elements.

CRediT authorship contribution statement

Gustavo Asai: Writing – review & editing, Writing – original draft, Methodology, Investigation, Formal analysis, Data curation, Conceptualization. **Chintan Jansari:** Writing – review & editing, Formal analysis. **Frédéric Lachaud:** Writing – review & editing, Writing – original draft, Supervision, Investigation, Formal analysis, Conceptualization. **Kunal Masania:** Writing – review & editing, Writing – original draft, Supervision, Formal analysis, Conceptualization. **Joseph Morlier:** Writing – review & editing, Writing – original draft, Supervision, Project administration, Funding acquisition, Formal analysis, Conceptualization.

Declaration of competing interest

The authors declare that they have no known competing financial interests or personal relationships that could have appeared to influence the work reported in this paper.

Acknowledgments

The authors acknowledge the support from Alexandre Coelho on the numerical code development. This study was financed in part by the Coordenação de Aperfeiçoamento de Pessoal de Nível Superior - Brasil (CAPES) - Finance Code 001. In addition, Kunal Masania and Chintan Jansari from the Delft University of Technology acknowledge the funding from the National Growth Fund Program NXTGEN HIGHTECH, Netherlands.

Appendix. Convergence analysis

Fig. A.13 shows the objective function and the history of the penalization factor for a flax/PLA design, to be printed in the direction $+z$. Convergence is reached after 42 iterations, with $p = 3$ and 16.3% of grey elements ($0.1 < \rho_e < 0.9$).

Fig. A.14 shows the history of the value of the volume fraction constraint function, see the mathematical problem formulation in (4). The densities are initially set as equal to the prescribed volume fraction

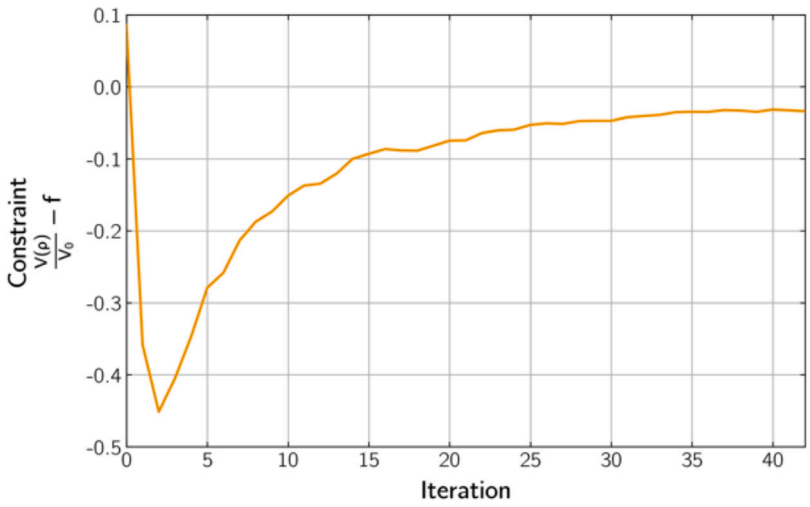

Fig. A.14. Evolution of the constraint function $V(\rho)/V_0 - f$ through the iterations. Material is removed in the first iterations and then slowly reallocated during the following iterations.

($f = 0.2$) in all elements, except in the regions near the boundaries, where the densities are fixed at 1. This leads to a violation of the constraint before the first iteration, which is quickly corrected by globally removing material, seen in the compliance history as an increase in compliance.

Data availability

The code for reproducing all analyses and optimizations is available at https://github.com/mid2SUPAERO/SOMP_Ansys.

References

[1] Sigmund O. A 99 line topology optimization code written in matlab. Struct Multidiscip Optim 2001;21:120–7. http://dx.doi.org/10.1007/s001580050176.

[2] Langelaar M. Topology optimization of 3D self-supporting structures for additive manufacturing. Addit Manuf 2016;12:60–70. http://dx.doi.org/10.1016/j.addma.2016.06.010.

[3] Duriez E, Morlier J, Azzaro-Pantel C, Charlotte M. Ecodesign with topology optimization. Procedia CIRP 2022;109:454–9. http://dx.doi.org/10.1016/j.procir.2022.05.278.

[4] Stromberg N. An efficient tradeoff approach for topology optimization with manufacturing constraints. In: International design engineering technical conferences and computers and information in engineering conference. vol. 44090, 2010, p. 1171–9. http://dx.doi.org/10.1115/DETC2010-28411.

[5] Papapetrou VS, Patel C, Tamijani AY. Stiffness-based optimization framework for the topology and fiber paths of continuous fiber composites. Composites B 2020;183:107681. http://dx.doi.org/10.1016/j.compositesb.2019.107681.

[6] Huang Y, Tian X, Zheng Z, Li D, Malakhov AV, Polilov AN. Multiscale concurrent design and 3D printing of continuous fiber reinforced thermoplastic composites with optimized fiber trajectory and topological structure. Compos Struct 2022;285:115241. http://dx.doi.org/10.1016/j.compstruct.2022.115241.

[7] Fang G, Zhang T, Huang Y, Zhang Z, Masania K, Wang CC. Exceptional mechanical performance by spatial printing with continuous fiber: Curved slicing, toolpath generation and physical verification. Addit Manuf 2024;104048. http://dx.doi.org/10.1016/j.addma.2024.104048.

[8] Kellens K, Mertens R, Paraskevas D, Dewulf W, Duflou JR. Environmental impact of additive manufacturing processes: does AM contribute to a more sustainable way of part manufacturing? Procedia CIRP 2017;61:582–7.

[9] Tang Y, Mak K, Zhao YF. A framework to reduce product environmental impact through design optimization for additive manufacturing. J Clean Prod 2016;137:1560–72.

[10] Duriez E, Azzaro-Pantel C, Morlier J, Charlotte M. A fast method of material, design and process eco-selection via topology optimization, for additive manufactured structures. Clean Environ Syst 2023;9:100114. http://dx.doi.org/10.1016/j.cesys.2023.100114.

[11] Castro Almeida A, Duriez E, Lachaud F, Morlier J. New topology optimization for low CO_2 footprint AFP composite structures. 2023, Poster session WCSMO.

[12] Agrawal T. Designing eco-efficient structures using multi-material topology optimization [Master's thesis], Delft University of Technology; 2024.

[13] Joshi SV, Drzal L, Mohanty A, Arora S. Are natural fiber composites environmentally superior to glass fiber reinforced composites? Composites A 2004;35(3):371–6.

[14] Song YS, Youn JR, Gutowski TG. Life cycle energy analysis of fiber-reinforced composites. Composites A 2009;40(8):1257–65.

[15] Dicker MP, Duckworth PF, Baker AB, Francois G, Hazzard MK, Weaver PM. Green composites: A review of material attributes and complementary applications. Composites A 2014;56:280–9.

[16] Pickering KL, Efendy MA, Le TM. A review of recent developments in natural fibre composites and their mechanical performance. Composites A 2016;83:98–112.

[17] Bendsøe MP. Optimization of structural topology, shape, and material. Berlin, Heidelberg: Springer Berlin Heidelberg; 1995, http://dx.doi.org/10.1007/978-3-662-03115-5.

[18] Sigmund O, Petersson J. Numerical instabilities in topology optimization: A survey on procedures dealing with checkerboards, mesh-dependencies and local minima. Struct Optim 1998;16(1):68–75. http://dx.doi.org/10.1007/BF01214002.

[19] Sigmund O, Maute K. Topology optimization approaches. Struct Multidiscip Optim 2013;48(6):1031–55. http://dx.doi.org/10.1007/s00158-013-0978-6.

[20] Bendsøe MP, Sigmund O. Material interpolation schemes in topology optimization. Arch Appl Mech 1999;69(9):635–54. http://dx.doi.org/10.1007/s004190050248.

[21] Lee J, Kim D, Nomura T, Dede EM, Yoo J. Topology optimization for continuous and discrete orientation design of functionally graded fiber-reinforced composite structures. Compos Struct 2018;201:217–33. http://dx.doi.org/10.1016/j.compstruct.2018.06.020.

[22] Kim D, Lee J, Nomura T, Dede EM, Yoo J, Min S. Topology optimization of functionally graded anisotropic composite structures using homogenization design method. Comput Methods Appl Mech Engrg 2020;369:113220. http://dx.doi.org/10.1016/j.cma.2020.113220.

[23] Li H, Gao L, Li H, Li X, Tong H. Full-scale topology optimization for fiber-reinforced structures with continuous fiber paths. Comput Methods Appl Mech Engrg 2021;377:113668. http://dx.doi.org/10.1016/j.cma.2021.113668.

[24] Stegmann J, Lund E. Discrete material optimization of general composite shell structures. Internat J Numer Methods Engrg 2005;62(14):2009–27.

[25] Zowe J, Kočvara M, Bendsøe MP. Free material optimization via mathematical programming. Math Program 1997;79(1):445–66.

[26] Jiang D. Three dimensional topology optimization with orthotropic material orientation design for additive manufacturing structures [Master's thesis], Baylor University; 2017.

[27] Hoglund RM. An anisotropic topology optimization method for carbon fiber-reinforced fused filament fabrication [Master's thesis], Baylor University; 2016.

[28] Jiang D, Hoglund R, Smith DE. Continuous fiber angle topology optimization for polymer composite deposition additive manufacturing applications. Fibers 2019;7(2):14. http://dx.doi.org/10.3390/fib7020014.

[29] Nomura T, Dede EM, Lee J, Yamasaki S, Matsumori T, Kawamoto A, Kikuchi N. General topology optimization method with continuous and discrete orientation design using isoparametric projection. Internat J Numer Methods Engrg 2015;101(8):571–605. http://dx.doi.org/10.1002/nme.4799.

[30] Stragiotti E. Continuous fiber path planning algorithm for 3D printed optimal mechanical properties [Master's thesis], Politecnico di Torino; 2020.

[31] Jantos DR, Hackl K, Junker P. Topology optimization with anisotropic materials, including a filter to smooth fiber pathways. Struct Multidiscip Optim 2020;61:2135–54. http://dx.doi.org/10.1007/s00158-019-02461-x.

[32] Schmidt M-P, Couret L, Gout C, Pedersen CB. Structural topology optimization with smoothly varying fiber orientations. Struct Multidiscip Optim 2020;62:3105–26. http://dx.doi.org/10.1007/s00158-020-02657-6.

[33] Qiu Z, Li Q, Luo Y, Liu S. Concurrent topology and fiber orientation optimization method for fiber-reinforced composites based on composite additive manufacturing. Comput Methods Appl Mech Engrg 2022;395:114962. http://dx.doi.org/10.1016/j.cma.2022.114962.

[34] Li Y, Ge W, Liu B, Wang Z, Jin S, Dong D. Collaborative optimization for variable stiffness composite laminates using a fiber angle description method based on Archimedean spiral function. Compos Struct 2024;329:117478. http://dx.doi.org/10.1016/j.compstruct.2023.117478.

[35] Smith H, Norato JA. Topology optimization with discrete geometric components made of composite materials. Comput Methods Appl Mech Engrg 2021;376:113582. http://dx.doi.org/10.1016/j.cma.2020.113582.

[36] Greifenstein J, Letournel E, Stingl M, Wein F. Efficient spline design via feature-mapping for continuous fiber-reinforced structures. Struct Multidiscip Optim 2023;66(5):99. http://dx.doi.org/10.1007/s00158-023-03534-8.

[37] Wang S, Liu J, He Z, Yang D. Concurrent optimisation of structural topology and fibre paths for 3D printing of continuous fibre composites based on chain primitive projection. Composites A 2024;185:108333.

[38] Jia D, Liu L, Zhu J, Zhang Y, Toropov V. Feature-driven topology optimization method preserving component sequences considering turning angle constraint. Acta Mech Sin 2024;40(10):423433.

[39] Chandrasekhar A, Kumar T, Suresh K. Build optimization of fiber-reinforced additively manufactured components. Struct Multidiscip Optim 2020;61:77–90.

[40] Ypsilantis K-I, Kazakis G, Faes MG, Ivens J, Lagaros ND, Moens D. A topology-based in-plane filtering technique for the combined topology and discrete fiber orientation optimization. Comput Methods Appl Mech Engrg 2023;417:116400. http://dx.doi.org/10.1016/j.cma.2023.116400.

[41] Woigk W, Fuentes C, Rion J, Hegemann D, Van Vuure AW, Dransfeld C, Masania K. Interface properties and their effect on the mechanical performance of flax fibre thermoplastic composites. Composites A 2019;122:8–17.

[42] Defoirdt N, Biswas S, De Vriese L, Van Acker J, Ahsan Q, Gorbatikh L, Van Vuure A, Verpoest I, et al. Assessment of the tensile properties of coir, bamboo and jute fibre. Composites A 2010;41(5):588–95.

[43] Christensen RM. Tensor transformations and failure criteria for the analysis of fiber composite materials. J Compos Mater 1988;22(9):874–97. http://dx.doi.org/10.1177/002199838802200906.

[44] Svanberg K. The method of moving asymptotes—a new method for structural optimization. Int J Numer Methods Eng 1987;24(2):359–73. http://dx.doi.org/10.1002/nme.1620240207.

[45] Kaszynski A, Derrick J, German, natter1, Kaszynski A, FredAns, jleonatti, simon-marwitz, 1081, Correia D, Addy D, JackGuyver, jazztekk, jkbgbr, spectereye. pyansys/pymapdl: v0.60.3. 2021, http://dx.doi.org/10.5281/zenodo.5726008.

[46] Gaynor AT, Guest JK. Topology optimization considering overhang constraints: Eliminating sacrificial support material in additive manufacturing through design. Struct Multidiscip Optim 2016;54(5):1157–72. http://dx.doi.org/10.1007/s00158-016-1551-x.

[47] GrabCAD. GrabCAD GE jet engine bracket challenge. 2013, URL: https://grabcad.com/challenges/ge-jet-engine-bracket-challenge. [Accessed 07 July 2023].

[48] ANSYS, Inc. Ansys GRANTA EduPack software. 2024, URL: https://www.ansys.com/materials.